Experimental study of particle impact on cohesive granular packing

H. Selmani, Jean-Baptiste Besnard, Ahmed Ould El Moctar, Pascal Dupont, Alexandre Valance

.

Experimental study of particle impact on cohesive granular packing

H. Selmani,[1] J. B. Besnard,[2] A. Ould El Moctar,[2] P. Dupont,[3] and A. Valance[4]

[1] *Institut d'Optique et Mécanique de Précision, Université Ferhat Abbas Sétif, Algérie.*
[2] *Univ Nantes, CNRS, Laboratoire Thermique et Energie de Nantes, UMR 6607, 44306 Nantes, France.*
[3] *Univ Rennes, INSA Rennes, LGCGM, 35043 Rennes, France.*
[4] *Univ Rennes, CNRS, Institut de Physique de Rennes, UMR 6251, Rennes, France.*

(Dated: November 22, 2024)

We investigate experimentally the impact process of sand particles onto a cohesive granular packing made of similar particles. We use sand-oil mixture with varying liquid content to tune the cohesive strength of the packing. The outcome of the impact is analyzed in terms of the production of ejected particles from the packing. We quantify this production as a function of the impact velocity of the particles for increasing cohesion strength. We identified three different regimes depending on the cohesion number Co, defined as the ratio of the inter-particle cohesive force to the particle weight. For small cohesion (i.e., $Co \lessapprox 1$), the ejection process is not modified by the cohesion. For intermediate cohesion (i.e., $1 \lessapprox Co \lessapprox 20$), the ejection process becomes less efficient: the number of ejected particles per impact for a given impact velocity is decreased but the critical impact velocity to trigger the ejection process remains unchanged. Finally, for strong cohesion (i.e. $Co \gtrapprox 20$), we observed a progressive increase of the critical impact velocity. These experimental results confirm spectacularly the outcomes of recent numerical simulations on the collision process of a particle onto a cohesive packing and open new avenues to model the aeolian transport of moist sand.

I. INTRODUCTION

In many physical and geophysical systems, the process of a particle impacting upon a granular substrate is an essential issue. As an example, the impact process has been recognized as the heart of aeolian saltation physics for wind-blown sand and snow [1–5]. In saltation transport, particles experience successive rebounds: they are accelerated by the wind in the ascending phase and when they return to the bed, they rebound and eject other particles from the bed. This impact process including the rebound and the ejection of particles is often referred to as "the splash process" and has been extensively investigated through model collision experiments [6–10] and numerical simulations [11–13]. These investigations have led to a fairly sound knowledge of the splash process in a situation of cohesion-less granular beds. In-situ studies of the splash process (i.e., field or wind-tunnel transport experiments) are very few [14, 15]: it is indeed challenging to investigate the collision process in a fully developed saltation regime because it is difficult to identify the result of a single impact due to the fact that many collisions occur at the same time within a unit bed surface area.

Another challenging issue is the collision process on a cohesive granular packing which takes place in aeolian transport of wet sand or snow [5, 16]. When adding even a small amount of liquid, the mechanical properties of the sand change dramatically. Although the formation of liquid capillary bridges between the grains [17–19] has been recognized to play an important role in this change, there is still no satisfactory theory to describe accurately the mechanical properties of wet granular media [20–22]. The snow is also a granular material with mechanical properties exhibiting an even more complexity than wet sand [23]. The cohesive properties of snow particles results from the formation of icy bonds, a process called sintering.

While the binary collision of cohesive particles [24] or collision between a particle and a wet surface [25, 26] has received some attention, very few studies investigate the collision process of a particle onto a cohesive granular packing. We can mention two numerical studies: The one by Ralaiarisoa et al. [27] in the context of capillary cohesion and the other by Comola et al. [5] in the situation of snow packing made cohesive with ice bridges. Ralaiarisoa et al. [27] studied the impact process through 2D Discrete element method (DEM) simulations on cohesive granular packing where the cohesion is ensured by water capillary bonds. An interesting finding is that when the cohesion number surpasses a critical value of order of 1, the ejection process is less efficient, that is the number of ejected particles per impact decreases, and the critical impact velocity to trigger the ejection is increased. Comola et al. [5] incorporated a cohesive force into a numerical 3D DEM-based model of aeolian transport of snow. In their study, the inter-particle cohesion is intended to describe the mechanics of icy solid bridges. A careful inspection of their results on the ejection process showed a qualitative agreement with the outcomes of [27], although both simulations differ by the nature of the cohesion (solid vs liquid bridge) and the space dimension (3D vs 2D).

To our knowledge, there is only one experimental study on the impact process with a cohesive bed: the one from Besnard et al. [28] who performed impact experiments with a cohesive sand bed but within a limited range of the cohesion strength precluding of a conclusive comparison with the simulation outcomes of [27]. In the present ar-

ticle, we extend the work in [28] by varying the cohesion strength over a much larger range. Our experimental results spectacularly validate the numerical results in [27] and indicate clearly the existence of two distinct critical cohesion numbers: The first corresponds to the decrease of the splash efficiency (diminution of the number of ejected particles) and the second to the threshold at which the critical impact speed for triggering the splash is modified by the cohesion.

The article is organized as follows: Section II describes the experimental setup and the protocols for characterizing the degree of cohesion of the granular bed and investigating the collision process. The effect of cohesion on the splash process is presented in Section III. A comparison between experimental results and numerical outcomes from Ralaiarisoa et al. [27] is presented in Section IV. Finally, we discuss the implication of our results on aeolian transport in the context of cohesive materials in Section V and conclude in Section VI

II. EXPERIMENTAL SETUP AND METHODOLOGY

A. Wind tunnel facility

The experiments were conducted in a wind tunnel with a working section length of 6.6 m and a cross-sectional area of 0.245 m × 0.27 m (see Fig. 1). As a cohesive sand bed, we employed a mixture of sand (with a mean diameter $d = 0.2$ mm and a density $\rho_p = 2650$ kg/m^3; see further details in Appendix A) and silicone oil (AR 20) with a surface tension of $\Gamma = 20.6 \times 10^{-3}$ N/m. The sand bed is confined into a box with a square section of 15 cm × 15 cm and a depth of 2 cm. The sand bed is displayed 5.6 m downstream from the wind tunnel's entrance and its vertical position is adjusted in order that the top surface of the packing is level with the floor of the tunnel. The latter is made rough by gluing sand particles of the same nature as those from the mixture. The sand bed is weighed continuously during the experiment by means of a scale with a milligram accuracy.

It is worth emphasizing that the sand bed level is adjusted at the beginning of each experiment. During an experiment which lasts typically between 5 to 10 minutes, the eroded mass represents less than a single grain layer such that the sand bed level is barely modified.

We made two types of experiments with distinct upstream conditions: (i) one with a small upstream particle flow rate Q_{in} and (ii) the other with no upstream particle. The former configuration is employed to assess the sand bed erosion rate due to particle impact and the latter to determine the strength of the cohesive mixture.

The air flow velocity in the tunnel can be varied over a large range of friction velocity u^* (typically from 0 to 1.2 m/s). The air flow velocity profile downstream the sand bed, $U(z)$, was characterized with Pitot tubes and was found to obey a classical logarithmic law

$$U(z) = \frac{u^*}{\kappa} \ln \frac{z}{z_0} \tag{1}$$

where κ is the Von Karman constant ($\kappa = 0.41$). The friction speed u^* follows a linear trend with the free stream velocity U_∞ ($u^* \approx 0.0388\, U_\infty$) and the aerodynamic roughness length z_0 is roughly constant and equal to $z_0 \approx 4.10^{-6}$ m $\approx d/50$.

B. Sand-oil mixture

We used basically the same protocol as done in[28] for elaborating the sand-oil mixture. We made several mixtures with increasing liquid content ω ranging from 0.1% to 3%. In the experiments made by Besnard et al. [28], the range of liquid was much less since the highest liquid content was $\omega = 0.4\%$.

It is worth underlying that the range of liquid content investigated in our paper corresponds to low liquid content (i.e., the pendular regime [19]) where the macroscopic cohesion strength greatly varis with liquid content.

TABLE I. Properties of the oil-sand mixtures including the liquid content ω (in percentage of mass), Ω (in percentage of volume), the packing fraction ϕ and the cohesion number Co (see section II.C for its definition and determination).

ω	0.	0.1	0.2	0.3	0.4	0.6	0.8	1	1.5	2	3
Ω	0.	0.27	0.53	0.8	1.06	1.59	2.12	2.65	3.98	5.3	7.95
Φ	0.58	0.58	0.55	0.52	0.52	0.52	0.52	0.52	0.52	0.52	0.52
Co	0.	0.5	1.3	2.3	3.5	6.6	10.7	15.8	32.6	55.2	118.3

Each mixture was prepared in a large container and homogenized manually using a metal rod. The mixture was then poured layer by layer into the dedicated box. Each layer was about 5 mm height and was smoothed out by a level rake before pouring the next layer.

This procedure leads to slightly different degrees of filling depending on the liquid content. For dry sand, the box was filled with a mass $M_0 \approx 600$ g (corresponding to a volume fraction $\phi \approx 0.58$) while for mixtures with liquid content ω greater or equal than 0.3, it was filled with a mass $M_0 \approx 500$ g leading to a smaller volume fraction $\phi \approx 0.52$ (see Table I).

C. Cohesion strength of the sand bed

To assess the cohesion strength of the sand bed, we conducted wind-tunnel experiments aiming to determine the aerodynamic erosion threshold. To do so, we evaluated the critical friction speed u^*_{sw} above which the sand is eroded by a turbulent air flow free of particles as a function of the liquid content ω. We used the same method as that employed in [28]. We determined the aerodynamic erosion rate E_{aero} by weighing the sand bed after

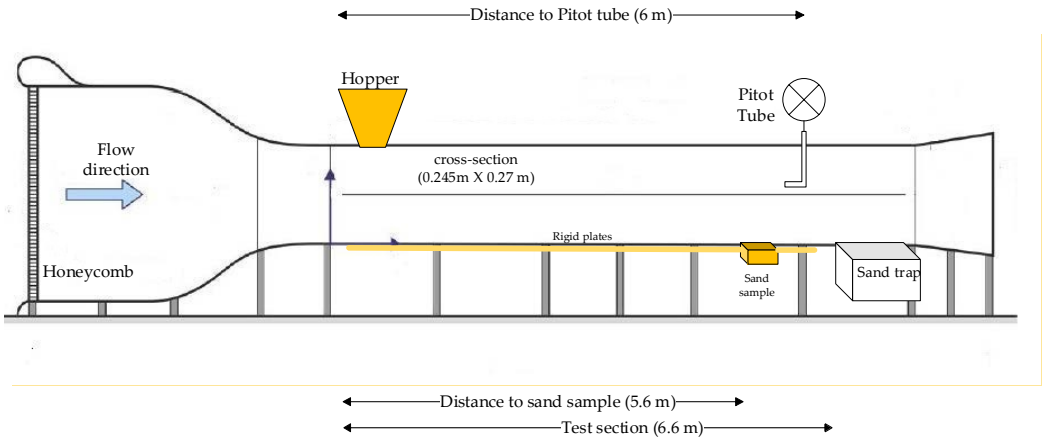

FIG. 1. Schematic view of the Wind tunnel.

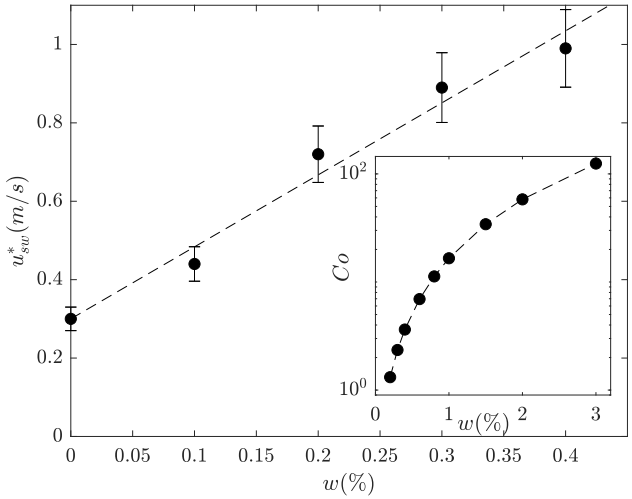

FIG. 2. aerodynamic erosion threshold u^*_{sw} as a function of the liquid content w. The dashed line corresponds to a linear fit to the data (see Eq.2). Inset: The cohesion number Co as a function of the liquid content. The cohesion number Co is obtained from Eq. 4. The dashed line corresponds to the predicted cohesion strength computed from the linear relationship between the threshold friction velocity and the liquid content.

1 minute of air flow as a function of the air flow strength and inferred u^*_{sw} when the erosion rate exceeds a small but finite value $E_{aero} \approx 5.10^{-3}$ g/m^{2}s. The procedure is detailed in Appendix B. The evolution of u^*_{sw} as a function of the liquid content ω is presented in Fig. 2. We confirm the result from [28] who found a linear variation with ω:

$$u^*_{sw} = u^*_s(1 + a_\omega \omega) \tag{2}$$

with $u^*_s \approx 0.3$ m/s and $a_\omega \approx 6$. The value of a_w is a bit lower than that found by [28] which was 7. We believe we have a better estimate of the regression slope since the latter is estimated over a larger range of liquid content. Our highest value of ω is 0.4% while in [28] it was 0.2%. Importantly, we could not determine the critical friction speed of erosion for liquid content greater than 0.4% because it requires wind speed beyond the capability of the wind tunnel fan. For $\omega = 0.4\%$, u^*_{sw} is about 1.2 m/s which corresponds to a nominal velocity $U_\infty \approx 35$ m/s.

From the aerodynamic threshold, we can infer a cohesive force F_c using a force balance at incipient motion as done by McKenna-Neuman and Nickling [29]:

$$\begin{aligned} F_c &\approx \frac{\pi}{18}\rho_p g d^3 \left(\left(\frac{u^*_{sw}}{u^*_s} \right)^2 - 1 \right) \\ &\approx \frac{\pi}{9}\rho_p g d^3 a_\omega \omega \left(1 + a_\omega \omega/2\right) \end{aligned} \tag{3}$$

F_c should be unterstood as an average inter-particle cohesive force and can a priori vary between 0 and the maximum capillary force (which is $\pi\Gamma d$ when two spheres at contact are bounded by a liquid meniscus) depending on the presence of liquid bonds at the grain contacts. The increase of F_c with the liquid content can be explained by the augmentation of the fraction of inter-particle contacts that have a liquid bonds [21]

From the estimation of F_c, we can define a dimensionless cohesion number Co, defined as the ratio of the average inter-particle cohesive F_c to the grain weight:

$$Co \equiv \frac{F_c}{(\pi/6)\rho_p g d^3} \tag{4}$$

We can deduce the cohesion strength in terms of the cohesion number Co. The values of the cohesion number as a function of the liquid content ω are reported in Table I. Note that for liquid content greater than 0.4, the values of the cohesion number are extrapolated using Eq. 3. The maximum cohesion number is reached when $F_c = \pi\Gamma d$ and corresponds to $Co = 115$ and $\omega \approx 3\%$.

D. Characterization of the splash process

The purpose of the experiments is to assess the impact erosion rate E_{impact} of the sand bed when it is impacted by sand particles. To do so, we impose a small but finite incoming particle flow rate Q_{in} at the entrance of the wind tunnel with the help of a hopper placed on the ceiling of the tunnel (see Fig. 1). The hopper delivers a fixed mass flow rate $Q_{in} = 0.67$ g/s. The released grains at the entrance of the wind tunnel experience a hopping motion over the upstream rigid bed, get quickly in equilibrium with the air flow and eventually impact the sand bed. For the impact process, two important parameters come into play: the mean particle impact velocity u_p and the vertical impacting flux Φ. Both parameters depend on the air flow strength. u_p increases with increasing air flow speed while Φ decreases. According to the measurement made by [30] in similar conditions, u_p and Φ are simply related to the air friction speed u^* by:

$$\frac{u_p}{\sqrt{gd}} \approx 80\left(\frac{u^*}{u^*_{reb}} - 1\right) \quad (5)$$

$$\Phi \approx 6.5\frac{Q_{in}}{(u^*/u^*_{reb} - 1)^2} \quad (6)$$

where u^*_{reb} is the critical shear velocity to sustain a steady saltation motion of a single grain on a rigid and rough bed ($u^*_{reb} \approx 0.128\,\mathrm{m/s}$). Below this critical shear velocity, particles start to deposit on the tunnel floor. The latter can be interpreted as the rebound threshold on a rigid bed [31, 32]. Experiments are run above this critical friction speed in order to ensure that the whole mass flux Q_{in} prescribed by the hopper at the entrance of the tunnel is transported along the wind-tunnel. In practice, we use air friction speeds greater or equal than $0.15\,\mathrm{m/s}$. Finally, it is important to stress that the above relations (Eqs. 5 and 6) hold as long as the flow is far from being saturated, that is, when the saltation layer is so dilute that the sand grains do not have any feed-back effect on the flow.

The impact erosion rate E_{imp} is determined by weighing the sand bed after a finite duration of particle impingement (typically between 1 and 2 minutes) and can be expressed as :

$$E_{imp} = \Phi \times N_E \quad (7)$$

where N_E is the average number of ejected grains per impact produced by impacting particles having an averaged velocity u_p. Our aim is to document how N_E changes both with increasing impact velocity and cohesion strength. The impact velocity is varied by tuning the air flow speed (Eq. 5) while the cohesion of the sand is increased by increasing the liquid content.

We should emphasize here that N_E is related to the number of ejected grains per impact as it was determined in splash experiments [33] or in numerical simulations [27]. In splash experiments and simulations, the number of ejected grains per impact, N_{ej}, is assessed for a well-controlled impact velocity ξ_p. In the present experiments, the impacting particles exhibit a finite dispersion around the mean value u_p. As shown in [27], one can infer $N_E(u_p)$ from $N_{ej}(\xi_p)$ if the velocity distribution of the impacting particle is known (see Appendix C for further details).

III. SPLASH PROCESS

The splash process was characterized through the impact erosion rate E_{imp}. The results are shown in Fig. 3. We plotted the rescaled erosion rate E_{imp}/Φ as a function of the dimensionless mean impact velocity $u_p/\sqrt{gd}$ (referred here after as the impact Froude number, $\mathcal{F}$) for different cohesion strengths.

A. Cohesionless case

We first discuss the cohesionless case. In this situation, the rescaled erosion rate can be well approximated by an affine function of the impact Froude number for a finite range of the Froude number: (i.e., $\mathcal{F}_c < \mathcal{F} < 70$).:

$$\frac{E_{imp}}{\Phi} \approx \mathcal{N}_0\,(\mathcal{F} - \mathcal{F}_c) \quad (8)$$

with $\mathcal{N}_0 = 0.065 \pm 0.005$ and $\mathcal{F}_c = 18 \pm 2$. $\mathcal{N}_0$ represents the impact efficiency and $\mathcal{F}_c$ is the critical value of the impact Froude number which can be interpreted as the onset of the ejection process. Below this value, there is no ejection of particles. The affine behavior breaks down for large Froude number (typically above 70): the increase of the impact erosion rate becomes non-linear with a power-law greater than 1. As already argued in [28], several mechanisms may act simultaneously to increase the efficiency of the measured erosion rate at high impact velocity. An additional contribution may result from the aerodynamic erosion and from a chain reaction process. As the bed has a finite size, the ejected grains may rebound several times before leaving the bed. If the latter are sufficiently accelerated by the wind, they can trigger other ejection events as they hit the bed as in a chain reaction process.

B. Influence of the cohesion

We then characterized how cohesion modifies the impact erosion process. The first salient feature of Fig. 3 is that the impact erosion rate keeps an affine behavior with the Froude number and can be still expressed in the form of Eq. 8 but with different values of the parameters $\mathcal{N}_0$ and $\mathcal{F}_c$ that vary with the cohesion strength. We can identify three distinct regimes for impact erosion as described below.

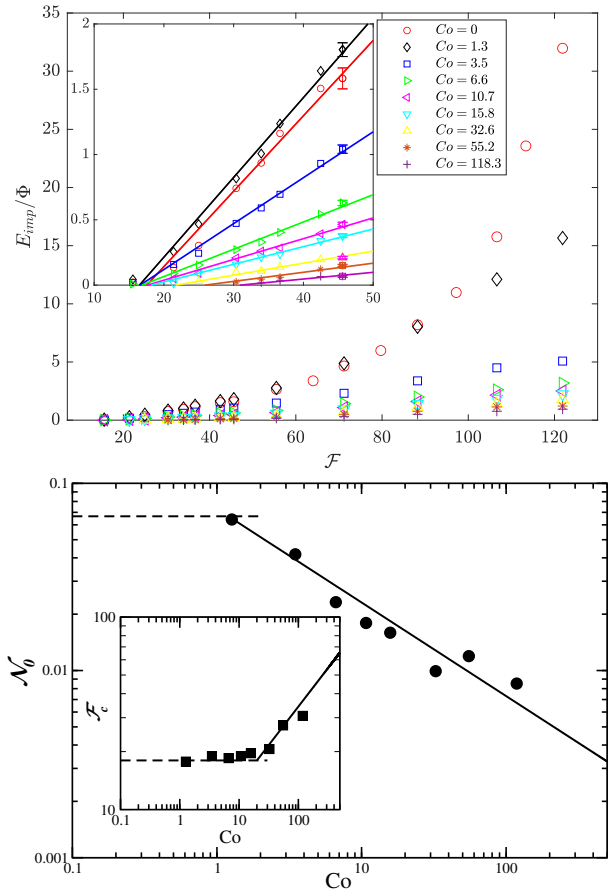

FIG. 3. (a) Rescaled impact erosion rate E_{imp}/Φ as a function of the Froude number for different cohesion numbers. Inset: Magnification for intermediate Froude number, underlining the linear trends of the impact erosion rate. (b) Variation of the slope $\mathcal{N}_0$ and the critical Froude number $\mathcal{F}_c$ (see inset) as a function of the cohesion number. $\mathcal{N}_0$ and $\mathcal{F}_c$ were determined within 10% accuracy

The horizontal dashed lines correspond to the cohesionless limit whereas the solid lines stand for the best fits using the following scaling laws: $\mathcal{N}_0 \propto Co^{-\alpha_1}$ and $\mathcal{F}_c \propto Co^{\alpha_2}$ with $\alpha_1 \approx 0.5$ and $\alpha_2 \approx 0.4$.

For low cohesion number (typically when $Co \leq Co_{c_1}$ with $Co_{c_1} \approx 1$), there is no significant change of the impact erosion rate: $\mathcal{N}_0$ and $\mathcal{F}_c$ are almost unchanged. Surprisingly, for the lowest value of cohesion (i.e., $Co = 1.3$), the impact efficiency $\mathcal{N}_0$ is however a little bit larger than in the cohesionless case (0.071 against 0.067). This feature has also been observed in [28]. This gives confidence that this is probably not an experimental artifact and could be explained by the gain of the energy stored in the liquid bridges.

For intermediate cohesion (i.e., $Co_{c_1} \leq Co \leq Co_{c_2}$ with $Co_{c_2} \approx 20$), the impact erosion becomes less efficient. The efficiency decrease is characterized by a diminution of the coefficient $\mathcal{N}_0$ while the critical impact Froude number $\mathcal{F}_c$ remains unchanged.

Finally for strong cohesion (i.e., $Co \geq Co_{c_2}$), impact erosion is severely mitigated both by a decrease of $\mathcal{N}_0$ and an increase of the critical impact Froude number $\mathcal{F}_c$.

As a summary, the experiments clearly exhibit three different regimes delineated by two distinct critical values of the cohesion number, $Co_{c_1} \approx 1$ and $Co_{c_2} \approx 20$. The first one corresponds to the critical cohesion value above which $\mathcal{N}_0$ starts to decrease and the second one to the critical value above which the threshold impact speed starts to increase. Figure 3.b depicts the evolution of $\mathcal{N}_0$ and $\mathcal{F}_c$ as a function of the cohesion number. A further analysis indicates that for $Co \geq Co_{c_1}$, $\mathcal{N}_0$ decreases as a power law of the cohesion number:

$$\mathcal{N}_0 = \mathcal{N}_0^{(0)} \left(\frac{Co}{Co_{c_1}} \right)^{-\alpha_1} \tag{9}$$

with $\alpha_1 \approx 0.5 \pm 0.05$ and $\mathcal{N}_0^{(0)} \approx 0.067$. $\mathcal{N}_0^{(0)}$ refers to the value obtained for a cohesionless bed. For $Co > Co_{c_2}$, the critical Froude number $\mathcal{F}_c$ follows as well a power law behavior with the cohesion number:

$$\mathcal{F}_c = \mathcal{F}_c^{(0)} \left(\frac{Co}{Co_{c_2}} \right)^{\alpha_2} \tag{10}$$

with $\alpha_2 \approx 0.4 \pm 0.05$ and $\mathcal{F}_c^{(0)} \approx 18$. $\mathcal{F}_c^{(0)}$ refers to the value obtained for a cohesionless bed. It is worth noting that the exponents α_1 and α_2 of the scaling laws are not so different and are close to the value 0.5. We will see that these scaling laws are in line with the numerical simulations by Ralaiarisoa et al. [27].

One final comment is worth mentioning. A careful inspection of the results indicate that the impact erosion rate can take negative values in a narrow range of the Froude number just below the critical Froude number $\mathcal{F}_c$ for strong cohesion (see Fig. 4). This means that there exists a regime where there is a net deposition of particles in the bed. In this regime, the trapping process of the bed overcomes the ejection process. As explained in Appendix C, the erosion rate results in a balance between the trapping and ejection processes. As predicted by the model exposed in the Appendix C, we expect a net deposition regime when $\mathcal{F} < \mathcal{F}_c$. The deposition regime is not observed for moderate cohesion because we are not able to conduct experiments with a sufficiently low Froude number without deposition over the upstream rigid bed (i.e. $u^* > u^*_{reb}$).

IV. COMPARISON WITH NUMERICAL SIMULATIONS

We compare in this section our experimental results with the numerical outcomes from Ralaiarisoa et al. [27]. They conducted two-dimensional simulations of the impact of a particle onto a cohesive granular packing using the discrete element method (DEM) to document the influence of the cohesion on the splash process. They considered granular packing made cohesive by the presence

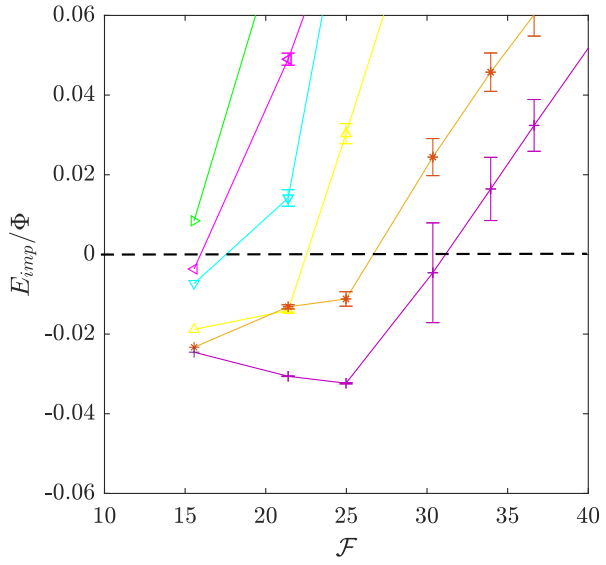

FIG. 4. Magnification of the impact erosion rate E_{imp} for Froude number ranging from 15 to 35, underlining the existence of a deposition regime (i.e., $E_{imp} < 0$).

of capillary bridges. The cohesion number was varied from 0 to 10^3 by increasing the inter-particle cohesion force via an augmentation of the liquid surface tension. The outcomes of the simulation are expressed in terms of the number of ejected particles per impact, N_{ej}, as a function of the impact speed ξ_p and exhibit the same qualitative trends as the experimental dimensionless impact erosion rate E_{imp}/Φ when the cohesion is increased. More precisely, $N_{ej}(\xi_p)$ is well approximated by an affine law of the same form as Eq. 8:

$$N_{ej} \approx N_0 \left[1 - e^2\right] (F - F_c) \tag{11}$$

with $N_0 \approx 0.62$ and $F_c \approx 12$ (see Appendix C). e is the effective restitution coefficient of the collision and depends on the impact angle θ (defined with respect to the horizontal) as $e = (A - B \sin\theta)$ with $A = 0.87$ and $B = 0.72$ (see Appendix C for further details). $F = \xi_p/\sqrt{gd}$ is the impact Froude number. The Froude number $\mathcal{F} = u_p/\sqrt{gd}$ calculated in the experiments differs from F. The former is an average calculated over the distribution of impact velocities ξ_p: $u_p = \langle \xi_p \rangle$ and $\mathcal{F} = \langle F \rangle$.

A re-analysis of the numerical data shows that N_0 does not evolve for $Co \leq Co'_{c_1} \approx 4$ and decreases for larger cohesion as a power law:

$$N_0 = N_0^{(0)} \left(\frac{Co}{Co'_{c_1}} \right)^{-\alpha'_1} \tag{12}$$

with $N_0^{(0)} \approx 0.61$ and $\alpha'_1 \approx 0.5$. Importantly, F_c remains unchanged for $Co \leq Co'_{c_2} \approx 10$ and increases for stronger cohesion as a power law:

$$F_c = F_c^{(0)} \left(\frac{Co}{Co'_{c_2}} \right)^{\alpha'_2} \tag{13}$$

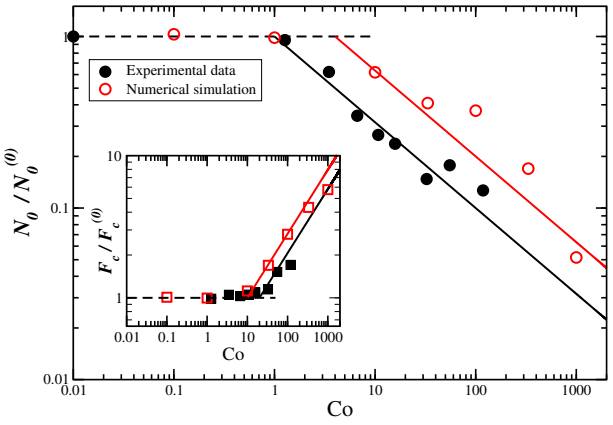

FIG. 5. Comparison of the slope $\mathcal{N}_0$ as a function of the cohesion number obtained from the experiments and the numerical simulations, respectively. Inset: Comparison of the critical Froude number $\mathcal{F}_c$ as a function of the cohesion number obtained from the experiments and the numerical simulations, respectively.

with $\alpha'_2 \approx 0.4$ and $F_c^{(0)} \approx 12$. It is worth mentioning that these numerical outcomes share the same qualitative features than those found by Comola et al. [5] and obtained in the context of snow where cohesion is ensured by icy bonds (see details in Appendix D).

The impact erosion rate E_{imp} can be deduced from the rate of ejection (see Eq. 11) as explained in Appendix C. The operation consists in making an average over the impact velocities ξ_p and yields:

$$\frac{E_{imp}}{\Phi} \approx \mathcal{N}'_0 \left(\mathcal{F} - \mathcal{F}'_c \right) \tag{14}$$

with

$$\mathcal{N}'_0 \approx a\, N_0 \,, \tag{15}$$

$$\mathcal{F}'_c \approx \frac{F_c}{2} \tag{16}$$

where a is a numerical constant (see Appendix C). Fig. 5 presents the evolution of $\mathcal{N}'_0$ and $\mathcal{F}'_c$ as a function of the cohesion number together with the experimental outcomes. The agreement between simulation and experiment is fairly good. There is a slight discrepancy in the regime transition and in particular for the critical values delineating the three regimes: $Co'_{c_1} \approx 4$ against $Co_{c_1} \approx 1$ and $Co'_{c_2} \approx 10$ against $Co_{c_2} \approx 20$. This difference may originate from the fact that the simulations were run in a two-dimensional configuration. However, the exponents of the scaling laws for $\mathcal{N}_0$ and $\mathcal{F}_c$ found in the simulation agrees well with those determined in the experiments.

V. DISCUSSION

The results obtained for aerodynamic and impact erosion open new avenues to figure out the different regimes

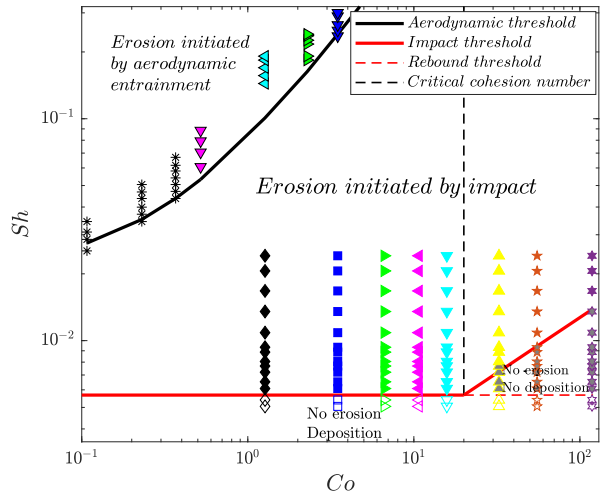

FIG. 6. Regime map in terms of the Shields number Sh versus the cohesion number Co. The symbols indicate the experimental values corresponding to the experiments. Boundaries between regimes of transport motion and no motion are indicated by solid red and black lines representing respectively the impact and aerodynamic thresholds

of aeolian sand transport occurring in the context of cohesive sand beds. From this perspective, it is instructive to translate our results in terms of the Shields number Sh (defined as $Sh = \rho_a u^{*2}/(\rho_p - \rho_a)gd$) that characterizes the strength of the flow instead of the impact Froude number. There is one to one relationship between the impact Froude number $\mathcal{F}$ and the friction velocity (or equivalently to the Shields number) through Eq. 5. Consequently the critical Froude numbers delimiting the regime transition can be expressed in the terms of the Shields number. Figure 6 pictures the regime map in terms of the Shields number and cohesion number. Distinct regimes of transport can be identified.

(i) At low Shields number (i.e., $Sh < 0.006$), there is no sustainable transport even for cohesionless sand. In this case, the air flow is not able to sustain sand transport and deposition occurs if the system is fed with sand.

(ii) For cohesion number less than 20, the threshold for impact erosion (red solid line in Fig. 6) is not modified by the cohesion and corresponds in terms of Shields number to a critical value $Sh_c = 0.006$. In this regime of cohesion, we expect the saturated sand transport rate to be identical to that found for cohesionless sand because the critical impact Froude number determines the saturated state of transport [34]. However, the threshold for aerodynamic erosion increases with increasing cohesion (black solid line), meaning that the direct erosion by the turbulent air flow demands higher and higher strength to trigger the transport in contrast with the impact erosion whose threshold is unchanged.

(iii) For greater cohesion number ($Co \geq 20$), the threshold for impact erosion is increased indicating that the splash process is significantly altered by the cohesion and the properties of the sand transport may be as well significantly modified.

A last important feature to note is the gap between the impact (red solid line) and aerodynamic (black solid line) erosion threshold is constantly increasing with increasing cohesion. The space region between the red and black solid line corresponds to conditions where the transport can be initiated only by the impact and not by aerodynamic entrainment. This region can be the site of hysteresis phenomena. The nature of the transport regime (absence or transport) will depend on initial and upstream boundary conditions. An other important related issue is the length needed for the transport to reach a saturated state in such conditions. Due to the decreasing efficiency of the splash process with increasing cohesion, we can expect much longer distance to reach a steady and fully-developed state and some potential restriction to assess such a state in finite wind-tunnel.

VI. CONCLUSION

An experimental finding indicates that the erosion threshold increases linearly with the liquid concentration. We do not have a physical explanation for this outcome. Numerous correlations, whether linear, logarithmic, or exponential, have been proposed in the literature. The majority of these correlations have been found for sand/water mixtures, where it can be challenging to guarantee that the water content would not change during the experiment. Here, we eliminate this uncertainty and demonstrate unequivocally that there is an affine correlation between the liquid content and the aerodynamic transport threshold when using a sand/oil mixture. We have conducted wind-tunnel experiments to document the collision process of an incident particle onto a cohesive granular packing of sand particles of 0.2 mm diameter mixed with silicon oil. Our experiments are the first ones investigating the role of cohesion in the collision process within a large range of cohesion strength. The latter reveals three distinct regimes of collision according to the cohesion strength. For moderate cohesion (i.e., $Co \leq 1$), the collision process remains unaffected by the cohesion. For intermediate cohesion (i.e., $1 \leq Co \leq 20$), the critical impact Froude F_c to trigger the ejection process is unchanged but the efficiency of the ejection process in terms of the rate of ejection (cf. the parameter N_0) is reduced severely. At high cohesion (i.e., $Co \geq 20$) both the critical impact Froude number F_c and the ejection rate N_0 are affected: F_c increases and N_0 decreases with increasing cohesion, both contributing to a diminution of the ejection efficiency. These experimental results are in line with recent numerical simulations [27] which gives confidence in the experimental outcomes.

These outcomes provide a complete picture of the splash process in the context of cohesive granular packing. We strongly believe that these results should open new avenues to better understand in particular aeolian

sand transport in the context of moist sand.

The last important point to be mentioned concerns the aerodynamic threshold which is found to increase linearly with the liquid content. Explaining the variation of the aerodynamic threshold with the liquid content from a microscopic force model remains an open issue that has to be addressed in the future.

Appendix A: Sand properties

We used natural quartz sand from Nemours (Sibelco NE34) with a density $\rho_p = 2650\,\mathrm{kg/m^3}$. Before use, we sieved it to remove dust and large residues. The laser diffraction analyis provides us with a median diameter $d = 200\,\mu\mathrm{m}$ (see Fig. A).

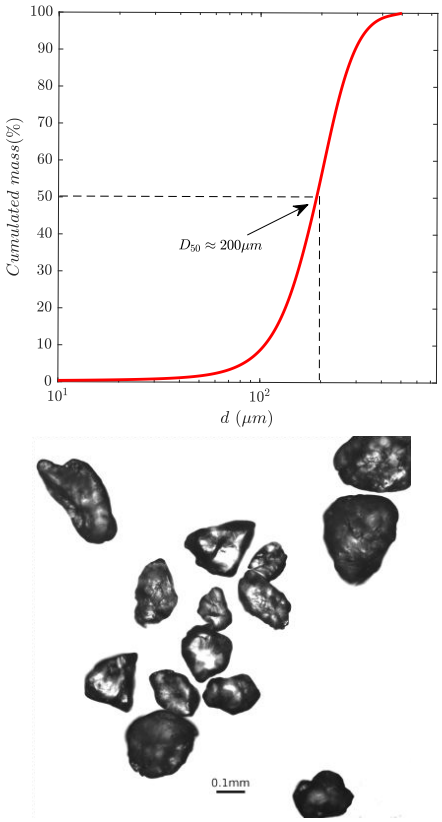

FIG. 7. (a) Cumulative distribution function of the particle size function obtained by laser diffraction analysis; (b) Photo of the sand grains

Appendix B: Aerodynamic erosion rate

To determine the aerodynamic threshold of our sand-oil mixture, we run similar experiments as for the impact erosion configuration but without feeding the wind-tunnel with sand. As a result, the sand-oil bed is eroded solely upon the action of the shearing of the turbulent air flow.

Figure 8 illustrates the variation of the erosion rate E with respect to the wind friction speed u^* for different liquid content ω ranging from 0.1% to 0.4%. In comparison with the experiments from [28], we explored a large range of liquid content. We confirm their results for liquid contents $w = 0.1$ and 0.2% and add two higher liquid contents: $w = 0.3$ and 0.4%. The aerodynamic erosion rate increases exponentially with the wind friction speed u^* for a given liquid content as shown in Fig. 8. This exponential increase is rather surprising and raises the issue concerning the criterion to define a meaningful aerodynamic threshold. As done in [28], we define the threshold when the erosion rate exceeds a critical value of $5.10^{-3}\,\mathrm{g/m^2.s}$. Over the duration of the experiment (about 5 minutes), it corresponds to an eroded mass of 0.034 g which is three times greater than the weight scale accuracy of 0.01 g.

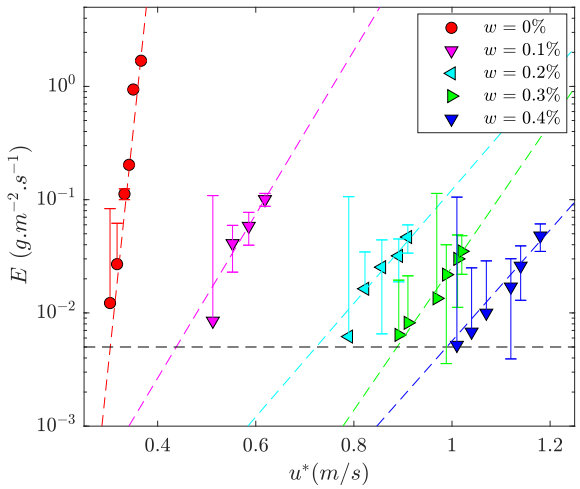

FIG. 8. Erosion rate E_{aero} as a function of the friction speed u^* for different liquid content ω. The lines represent exponential fits to the data whereas the horizontal dashed line stands for the critical value of the erosion rate used to define the threshold friction velocity to initiate transport.

Appendix C: Derivation of the impact erosion rate from the ejection process

We show here how to infer the impact erosion rate from the knowledge of the ejection process. We assume that the velocity distribution of the impact particles as well as the features of the ejection process are known.

Based on the numerical simulations and experiments [13, 27, 33], the number of particles, including the rebound, resulting from an impact at velocity ξ_p can be

modeled by:

$$N(\xi) = \begin{cases} 1 + N_{ej} & \text{if } \xi_p > \xi_c \\ 1 & \text{if } \xi_0 \leq \xi_p \leq \xi_c \\ 0 & \text{if } \xi_p \leq \xi_0, \end{cases} \quad \text{(C1)}$$

with

$$N_{ej}(\xi) = N_0(1 - (A - B\sin^2\theta)^2)\,(\xi_p - \xi_c)\,/\sqrt{gd} \quad \text{(C2)}$$

ξ_c is the critical velocity below which there is no ejection and $\xi_0 \approx \sqrt{gd}$ corresponds to the minimum particle impact velocity below which the particle is captured by the bed N_{ej} is the number of ejected grains per impact when $\xi_p \leq \xi_c$ and θ is the impact angle defined with respect to the horizontal. The experimental measurements for a 3D cohesionless granular packing give $A = 0.86$, $B = 0.72$, $N_0 \approx 0.32$ and $\xi_c \approx 40\sqrt{gd}$ [33]. The 2D numerical simulations of the collision process from Ralaiarisoa et al. [27] yields slightly different values for N_0 and ξ_c: $N_0 \approx 0.62$ and $\xi_c \approx 12\sqrt{gd}$ [27]. This difference comes from the 2D character of the numerical simulations.

As done in [35], it is reasonable to assume that the velocity of the impacting grains obeys a half-Gaussian distribution (i.e., $\xi_{py} < 0$):

$$f = \frac{c_0}{\pi\sqrt{T_x}\sqrt{T_y}} e^{-(\xi_{px}-u_p)^2/2T_x} e^{-\xi_{py}^2/2T_y}\,, \quad \text{(C3)}$$

where ξ_{px} and ξ_{py} are the horizontal and vertical components of the impact velocity $\vec{\xi_p}$ (ξ_{py} is negative for impacting particle), c_0 is the concentration of the impacting particle at the bed, u_p is the mean horizontal velocity of the impacting particles, $T_x = \langle(\xi_{px} - u_p)^2\rangle$ and $T_y = \langle\xi_{py}^2\rangle$.

With these assumptions, the impact erosion rate reads:

$$E_{imp} = m\int_{\xi_{py}<0} (N-1)\xi_{py} f(\vec{\xi_p}) d\vec{\xi_p} \quad \text{(C4)}$$

Following [35], the erosion rate can be split into two contributions: the rate of ejected grains, E_{ej}, and the rate of grains trapped by the bed, E_{loss}, which are given respectively by

$$E_{ej} = m\int_{\xi_{py}<0,\xi_p>\xi_c} f(\vec{\xi_p}) N_{ej}(\vec{\xi_p}) |\xi_{py}| d\vec{\xi_p}\,, \quad \text{(C5)}$$

$$E_{loss} = m\int_{\xi_{py}<0,\xi_p<\xi_0} f(\vec{\xi_p}) |\xi_{py}| d\vec{\xi_p}\,. \quad \text{(C6)}$$

The result of the integration yields [35]:

$$E_{ej} \approx \frac{mc_0N_0}{\pi\sqrt{T_xT_y}} \frac{T_x^3}{u_p(\xi_c - u_p)^2} e^{-(\xi_c-u_p)^2/2T_x} \times \left(1 - A^2 + AB\sqrt{\frac{2\pi T_x}{\xi_c u_p}}\right)\,, \quad \text{(C7)}$$

$$E_{loss} \approx 74\,\frac{mc_0}{\pi\sqrt{T_xT_y}}\,\xi_c^3 e^{-u_p^2/(2T_x)}\,. \quad \text{(C8)}$$

The impact erosion rate vanishes when E_{ej} balances exactly E_{loss}. Assuming that $u_p \gg \sqrt{T_x}$, the balance reduces to [35]:

$$u_p \approx \frac{\xi_c}{2} \quad \text{(C9)}$$

This means that the erosion rate vanishes when the mean particle velocity of the impacting particle equals half the mean critical velocity $u_c \approx \xi_c/2$. The critical mean particle velocity is thus completely linked to the critical impact velocity ξ_0 to trigger the ejection process. A linear expansion around u_c provides an approximate for the erosion rate which yields to first order:

$$E_{imp} \approx \phi\, N_0 \left(1 - A^2 + AB\sqrt{\frac{4\pi T_x}{\xi_c^2}}\right) \frac{T_x^{3/2} e^{-\xi_c^2/8T_x}}{\pi\xi_c T_y} \times (\mathcal{F} - \mathcal{F}_c) \quad \text{(C10)}$$

where $\phi = mc_0\sqrt{T_y}$ is the vertical impacting mass flux, $\mathcal{F} = u_p/\sqrt{gd}$ and $\mathcal{F}_c = \xi_c/2\sqrt{gd}$. If we take a typical value of T for saltation transport on a rigid and rough bed [30] ($T_x \approx T_y \approx 200\,gd$), we get:

$$\frac{E_{imp}}{\phi} \approx \mathcal{N}_0\,(\mathcal{F} - \mathcal{F}_c) \quad \text{(C11)}$$

with $\mathcal{N}_0 \approx aN_0$ and $\mathcal{F}_c \approx F_c/2$. a is a numerical constant that depends on ξ_c. For $\xi_c = 40\sqrt{gd}$, we get $a \approx 0.2$.

Appendix D: Numerical simulation of the splash process

It is instructive to compare the outcomes of numerical simulations of the splash process conducted in different contexts: the one by Ralaiarisoa et al. [27] that considers cohesion induced by liquid bonds and the other by Comola et al. [5] conducted in the context of snow transport where the particles are linked via solid bonds. The results of both types of simulations are presented in Fig. 9.

The number of the ejected particles as a function of the Froude number behaves similarly in both simulations as:

$$N_{ej} = N_0(1 - e^2)(F - F_c)\,, \quad \text{(D1)}$$

where N_0 and F_c depend only on the cohesion number Co. For both simulations, we can identify three different regimes: a first regime for weak cohesion numbers where the ejection process is not modified by the cohesion, an intermediate regime where N_0 decreases with increasing cohesion while F_c is unchanged, and a third regime for strong cohesion where N_0 continues to decrease and F_c starts to decrease with increasing cohesion. There is however a discrepancy in the critical cohesion numbers that delineate the regime transitions. In [27], we recall that the critical cohesion numbers are: $Co'_{c_1} \approx 4$

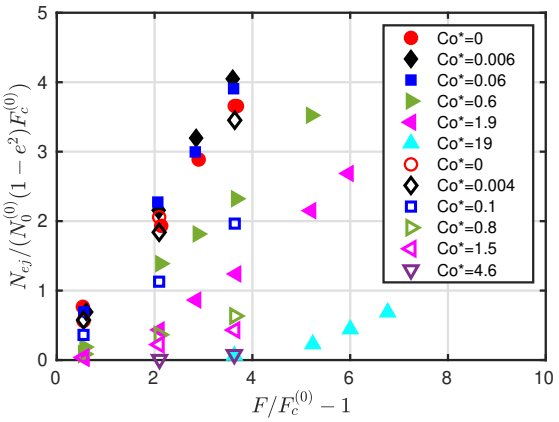

FIG. 9. Number of ejected particles per impact as a function of the impact Froude number for different cohesion number. Filled symbols: Data from [27] with $N_0^0 \approx 0.61$ and $F_c^{(0)} \approx 12$; Open symbols: data from [5] with $N_0^0 \approx 0.13$ and $F_c^{(0)} \approx 23$. $N_0^{(0}$ and $F_c^{(0)}$ refer to the values obtained for cohesionless bed (i.e., for $Co^* = 0$).

and $Co'_{c_2} \approx 10$. In contrast, the outcomes of Comola et al. [5] suggest different critical values: $Co'_{c_1} \approx 92$ and $Co'_{c_2} \approx 690$.

This disagreement raises the issue about the relevant parameter to characterize the cohesion strength. An alternative dimensionless parameter Co^* can be built from the energy W_{coh} necessary to break a cohesive bound:

$$Co^* \equiv \frac{W_{coh}}{mgd} \tag{D2}$$

with $W_{coh} \approx F_{coh} \times d_c/2$, where d_c is the critical distance between two neighbor particles above which the bound breaks. The two cohesion numbers are simply linked through the following relation:

$$Co^* = \frac{Co\, d_c}{2d} \tag{D3}$$

In [27], d_c is related to the volume V_l of the liquid meniscus (i.e., $d_c \approx V_l^{1/3}$) while in [5] d_c is determined via the cohesion force and the stiffness k of the spring used to model the icy bound (i.e., $d_c \approx F_{coh}/2k$). We can re-compute the critical values of the cohesion number in terms of Co^*. We get $Co^{*\prime}_{c_1} \approx 0.5$ and $Co^{*\prime}_{c_2} \approx 2$ for cohesive beds with capillary bounds and $Co^{*\prime}_{c_1} \approx 0.1$ and $Co^{*\prime}_{c_2} \approx 2$ for cohesive beds with icy bounds. The comparison of the critical values provides a much better agreement. This tells us that a cohesion number based on the energy necessary to break the bound is probably more relevant than a force-based cohesion number when the nature of the bound is different. An energetic description of the cohesion in the experiments is in principle possible but it requires a detailed knowledge of the properties of cohesive bridges at the grain scale. This is not the case in our experiments.

ACKNOWLEDGMENTS

H.S would like to acknowledge the financial support from "Institut de physique de Rennes" and "Ecole Polytechnique de Nantes" in the framework of an invited professor position. A.V., P.D and A.O.M acknowledge the support of the French Research National Agency through the project ANR-21-CE30-0066.

[1] R. A. Bagnold, *The Physics of Blown sand and Desert Dunes* (Methuen, New York, 1941).
[2] O. Duran, P. Claudin, and B. Andreotti, Aeolian Research **3**, 243 (2011).
[3] A. Valance, K. R. Rasmussen, A. Ould El Moctar, and P. Dupont, Comptes Rendus Physique **16**, 105 (2015).
[4] J. F. Kok, E. J. R. Parteli, T. I. Michaels, and D. B. Karam, Rep. Prog. Phys. **75**, 106901 (2012).
[5] F. Comola, J. Gaume, J. F. Kok, and M. Lehning, Geophys. Res. Lett. **46**, 5566 (2019).
[6] S. Mitha, M. Q. Tran, B. T. Werner, and P. K. Haff, Acta Mechanica **63**, 267 (1986).
[7] B. T. Werner, The Journal of Geology **98**, 1 (1990).
[8] F. Rioual, A. Valance, and D. Bideau, Phys. Rev. E **62**, 2450 (2000).
[9] D. Beladjine, M. Ammi, L. Oger, and A. Valance, Phys. Rev. E **75**, 061305 (2007).
[10] M. Ammi, L. Oger, D. Beladjine, and A. Valance, Phys. Rev. E **79**, 021305 (2009).
[11] B. T. Werner and P. K. Haff, Sedimentology **35**, 189 (1988).
[12] R. S. Anderson and P. K. Haff, in *Aeolian Grain Transport 1*, Vol. 1, edited by O. E. Barndorff-Nielsen and B. B. Willetts (Springer Vienna, Vienna, 1991) pp. 21–51.
[13] L. Oger, M. Ammi, A. Valance, and D. Beladjine, Eur. Phys. J. E **17**, 467 (2005).
[14] B. B. Willetts and M. A. Rice, Earth Surf Processes Landf **14**, 719 (1989).
[15] M. A. Rice, B. B. Willetts, and I. K. McEWAN, Sedimentology **43**, 21 (1996).
[16] S. L. Namikas and D. J. Sherman, *Desert Aeolian Processes* (Springer Netherlands, Dordrecht, 1995) pp. 269–293.
[17] O. Pitois, P. Moucheront, and X. Chateau, Journal of Colloid and Interface Science **231**, 26 (2000).
[18] L. Bocquet, E. Charlaix, and F. Restagno, Comptes Rendus. Physique **3**, 207 (2002).
[19] N. Mitarai and F. Nori, Advances in Physics **55**, 1 (2006).
[20] Z. Fournier, D. Geromichalos, S. Herminghaus, M. M. Kohonen, F. Mugele, M. Scheel, M. Schulz, B. Schulz, C. Schier, R. Seemann, and A. Skudelny, Journal of Physics: Condensed Matter **17**, S477 (2005).
[21] V. Richefeu, M. S. El Youssoufi, and F. Radjaï, Phys. Rev. E **73**, 051304 (2006).

[22] M. Scheel, R. Seemann, M. Brinkmann, M. Di Michiel, A. Sheppard, B. Breidenbach, and S. Herminghaus, Nature Materials **7**, 189 (2008).
[23] J. R. Blackford, Journal of Physics D: Applied Physics **40**, R355 (2007).
[24] C. M. Donahue, C. M. Hrenya, and R. H. Davis, Phys. Rev. Lett. **105**, 034501 (2010).
[25] S. Antonyuk, S. Heinrich, N. Deen, and H. Kuipers, Particuology **7**, 245 (2009), from micro-scale to technical dimension - Challenges in the simulation of dense gas-particle flows.
[26] T. Müller and K. Huang, Phys. Rev. E **93**, 042904 (2016).
[27] V. Ralaiarisoa, P. Dupont, A. O. E. Moctar, F. Naaim-Bouvet, L. Oger, and A. Valance, Phys. Rev. E **105**, 054902 (2022).
[28] J. Besnard, P. Dupont, A. Ould El Moctar, and A. Valance, JGR Earth Surface **127** (2022), 10.1029/2022JF006803.
[29] C. McKenna-Neuman and W. G. Nickling, Canadian Journal of Soil Science **69**, 79 (1989).
[30] T. D. Ho, *Experimental study of saltating particles in a turbulent boundary layer*, Ph.D. thesis, University of Rennes 1 (2012).
[31] T. Pähtz, A. H. Clark, M. Valyrakis, and O. Durán, Reviews of Geophysics **58**, e2019RG000679 (2020).
[32] T. Pähtz, Y. Liu, Y. Xia, P. Hu, Z. He, and K. Tholen, Journal of Geophysical Research: Earth Surface **126**, e2020JF005859 (2021).
[33] D. Beladjine, M. Ammi, A. Valance, and L. Oger, Physical Review E. **75**, 061305 (2007).
[34] J. T. Jenkins and A. Valance, Physics of Fluids **26**, 073301 (2014).
[35] M. Creyssels, P. Dupont, A. O. El Moctar, A. Valance, I. Cantat, J. T. Jenkins, J. M. Pasini, and K. R. Rasmussen, J. Fluid Mech. **625**, 47 (2009).